ACS APPLIED ELECTRONIC MATERIALS

pubs.acs.org/acsaelm
Article

Effective Conduction Path of a C_{60} Chain in a Nanogap Electrode

Masato Takei, Takuma Hirama, Hiroshi Suga,* Katsunori Wakabayashi, and Kazuhito Tsukagoshi*

Cite This: ACS Appl. Electron. Mater. 2024, 6, 1740−1745
Read Online

ACCESS | Metrics & More | Article Recommendations | Supporting Information

ABSTRACT: The electrical current path of fullerene-derived films between microfabricated sharpened metal electrodes (gaps of 10−20 nm) was evaluated. When a high voltage was applied, a space-charge-limited current (SCLC) flowed through the fullerene film. The effective conduction path length estimated from the SCLC voltage was slightly longer than the shortest distance between the electrodes. This indicates that the effective current path was tortuous because of the amorphous packing of the spherical fullerenes. Correlations between the effective path length and switching parameters such as operating voltages were used to show that the minimum operating power required for a minimum-sized fullerene switch is expected to be in the subpicowatt range.

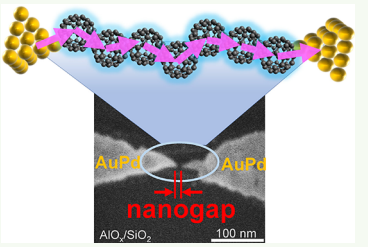

KEYWORDS: *fullerene, polymerization, C_{60} pyrrolidine tris-acid (CPTA), resistance switching, nanogap electrode, fullerene derivative, Poole−Frenkel effect, space-charge-limited current (SCLC)*

INTRODUCTION

A fundamental understanding of the effective electrical current path in electronic devices is useful for designing device structures and developing advanced functions.[1−3] For conductive channel materials with a sufficiently large size, current paths can be visualized using discharge phenomena caused by high-frequency magnetic fields.[4] When an electrical bias is applied, current is induced in the material, and its path is deformed. The deformed material along the current path can be observed by scanning electron microscopy (SEM) or transmission electron microscopy (TEM) imaging.[2,5−7] In addition, the deformed material trace can be spatially mapped using Raman spectroscopy.[8] For conductive media at the single-molecule scale, TEM images provide a direct visualization of the conductive channel, such as metallic atoms[9] bridging the gap between two metallic contacts or a fullerene dimer within the gap.[10] Computational image construction based on energy spectra is currently a powerful tool to precisely define the molecular-scale conduction channel.[11,12] However, when the conduction channel is placed on an insulating substrate and no clear trace of current flow in the material remains, it is extremely difficult to clarify the effective current path between the two electrodes.[13,14] In particular, material with a length of several nanometers exceeds the range of computational image construction, even though the phenomena occurring between electrodes can be understood.

When current flows between two sharpened electrodes, it is widely believed that the current is simply injected from the top of the electrode and flows through the medium at the shortest distance between the two electrodes. This assumption can be applied to large-scale channels and media with homogeneous elemental distributions. For media with countable particles within the conduction space, the current flows through the media via connections between adjacent particles.

In this study, we estimated the current path length by performing space-charge-limited current (SCLC) characterization of C_{60} chains within electrode gaps of different widths. The effective path length evaluated from the SCLC voltage was longer than that obtained from the SEM images. This is attributed to the tortuous path formed by the amorphous packing of spherical fullerenes. The characteristics of a very small switch element were inferred from the current path length, with respect to the switch characteristics observed for the C_{60} chains.

EXPERIMENTAL SECTION

We investigated the effective current path based on the SCLC conduction principle of fullerene.[15−23] This mechanism is reproducibly observed as a current flowing through a fullerene-derived film between electrodes under a high applied electric field.[24] Within the low-voltage regime, the dominant conduction mechanism of nanoscale C_{60} chains is Poole−Frenkel (PF) conduction, characterized by hopping conduction. When larger voltages are applied, SCLC is observed.[24] An SCLC occurs when the electron injection from the electrical contact to the conductive media exceeds the equilibrium concentration of the electrical current flow in the channel, limiting further electron injection.

Source and drain electrodes with nanogaps between them were fabricated using an electron beam lithography process and electromigration.[25] Gapless wire electrodes were fabricated by using thermal evaporation and lift-off techniques and were subsequently disconnected by electromigration (Figure 1a). A 10 nm-thick narrow

Received: November 25, 2023
Revised: February 7, 2024
Accepted: February 7, 2024
Published: February 26, 2024

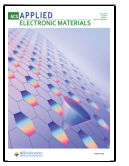

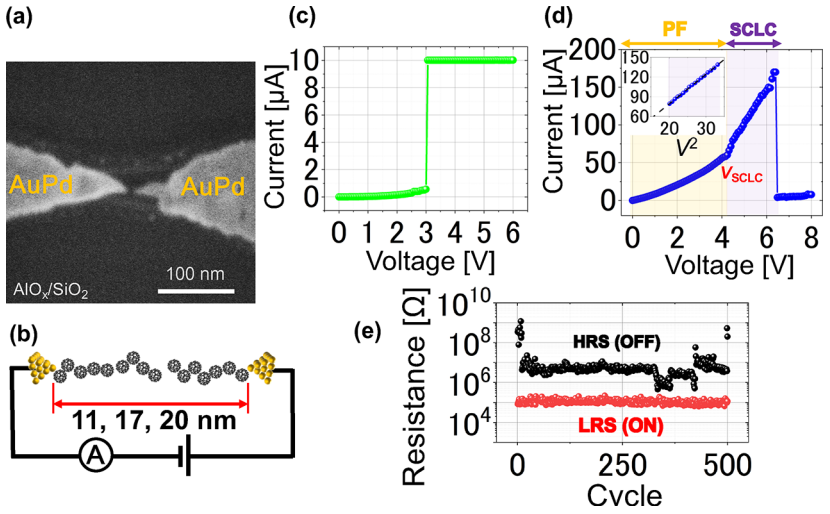

Figure 1. (a) SEM image (50 kV) of an 11 nm nanogap electrode (S channel device) formed by electron beam lithography. (b) Schematic of C_{60} chains bridging the electrode gap. I–V characteristics of (c) set with turn-on and (d) reset with NDR. Inset in panel (d): I–V^2 plot to visualize SCLC characteristics. (e) Sequential resistance changes were observed over 500 cycles of the input for panels (c, d).

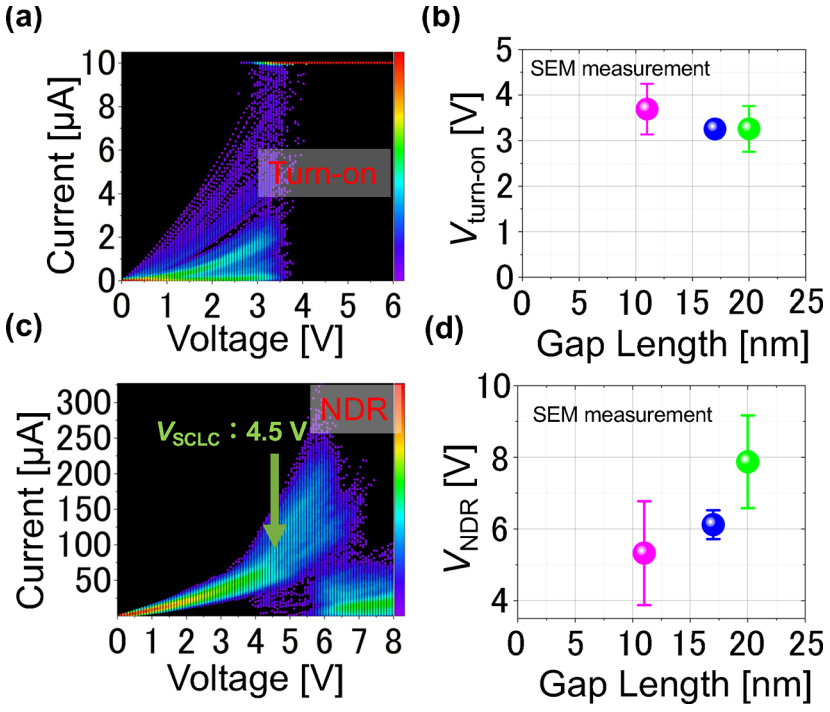

Figure 2. (a, b) Set and (c, d) reset characteristics in the M channel device. I–V plots for the (a) set and (c) reset operations plotted over 1000 measurements. (a) In the set operation, the current transition occurred at 3.4 V as a turn-on point from the LRS to HRS. (b) Turn-on voltage as a function of the gap width measured by the SEM. (c) Inflection point in the I–V plots at 4.5 V was taken as V_{SCLC}. (d) Average V_{NDR} as a function of the gap width measured by SEM.

AuPd wire (Au:Pd = 8:2) was prepared. Electromigration using the feedback scheme was then used to gently open the gap, and its feedback parameters, such as current limitation, were used to adjust the width of the gap. A variable gap is useful for characterizing the C_{60} nanochain length dependence. Three lengths of 11, 17, and 20 nm (as measured by SEM) were prepared. These three gaps are denoted as the short (S), medium (M), and long (L) channels. Although the gap width was carefully measured from the highly magnified SEM image, typical SEM images show a dim edge of a subnanometer object on a thick insulating substrate (Figure S1).[26] In addition to the surface conditions of the metallic electrode, the actual contact point with the nanoscale spherical fullerene could potentially be selected by using another current injection point near the top of the tip. Therefore, it is difficult to precisely define the actual current path from SEM images of the nanoscale electrode.

A Si substrate with a 250 nm SiO_2 film was coated with a 2 nm film of AlO_x by atomic layer deposition to allow C_{60} pyrrolidine tris-acid (CPTA) to be applied uniformly on the substrate surface.[14] CPTA dispersed in dimethylformamide was deposited by spin coating.[27] The thickness of a typical CPTA layer was 5 nm. The nanogap showed no current during I–V characterization before CPTA coating and showed reproducible currents after coating (Figure S2).

The actual diameter of C_{60} is 0.7 nm with a space of 0.37 nm between the C_{60} molecules,[28] which is similar to the typical layer spacing of graphite. Then, the C_{60} period was identified as

https://doi.org/10.1021/acsaelm.3c01656
ACS Appl. Electron. Mater. 2024, 6, 1740−1745

approximately 1.1 nm, indicating that the number of C_{60} molecules in the 17 nm gap was 16 or less.

In this study, a fullerene derivative of CPTA was used as the conductive channel material. Simple fullerenes such as C_{60} and C_{70} and variable endohedral fullerenes have been employed as single-molecule[29−33] or film[13−16,34−45] devices. In comparison with these fullerenes, CPTA has advantages such as oversolvability in solution and uniform adhesion on the substrate surface.[46] Thus, CPTA has been widely used as an efficient electron-transport layer in perovskite solar cells.[45] Because of the nanoscale short-range path of vertical transport in solar cells and in-plane transport in the case of our nanogap experiment, hopping conduction due to the PF effect could occur to generate a current flow.

Measurements (Figure 1b) were performed at room temperature and a pressure of 5.0×10^{-3} Pa. Electrical conductivity measurements were performed in a light-shielded chamber to avoid unintended exposure of the device to light. For the preset switching operation, a voltage was gradually applied between the electrodes by increasing it from zero. The current injected into the CPTA film from the electrode results in hopping conduction[23] because of the PF effect.[47] It should be noted that the CPTA film placed between sharpened metal electrodes with a 10−20 nm gap width did not require electron beam irradiation to preset the initial film conduction, whereas a large-area fullerene film required a preset polymerization process.

When a further voltage was applied, the current increased nonlinearly, promoting fullerene polymerization in the film between the two electrodes.[48,49] When a larger current is applied, a step-like current reduction in the $I-V$ characteristics occurs and the resistance between the electrodes becomes high. This decrease in current is termed negative differential resistance (NDR) and is denoted as a reset process. NDR can be understood as the current decrease when the C_{60} chain is disconnected, which is induced by the heat generated by the high current density, resulting in an increase in the two-terminal resistance. This condition can be regarded as a high-resistance state (HRS). When the voltage was applied again from zero, the current showed a step-like increase, and the two-terminal resistance changed to a low-resistance state (LRS) (Figure 1c). In this process, the C_{60} chain was reconnected between the two electrodes; when the voltage was applied to the LRS, the NDR occurred again (Figure 1e). This switching sequence can be cyclically repeated as the voltage input was cycled (Figure S3).[13,14,42,50] Further details can be found in a previous report.[24]

Figure 1c illustrates the $I-V$ characteristics of the set process, where the voltage was reapplied after the resistance increased owing to the NDR. During voltage application, SCLC occurred on the high-voltage regime following the PF effect in the low-voltage regime. SCLC and PF conduction were distinguished based on their different voltage characteristics. PF conduction was identified using a linear $I-V^{1/2}$ plot, whereas SCLC was characterized using a linear $I-V^2$ plot (inset of Figure 1d). The SCLC transition voltage (V_{SCLC}) is defined by the pronounced inflection point in the $I-V$ curves.

To obtain the statistical average V_{SCLC} value, the switch operation (Figure 1d) was repeated 1000 times, and the $I-V$ characteristics of the reset process were plotted (Figure 2a). All $I-V$ curves exhibited inflection points used to determine V_{SCLC} (marked by an arrow), proving that SCLC occurred in the narrow gap. The parts of the $I-V$ curves between V_{SCLC} and V_{NDR} (the voltage at which NDR occurs) exhibit SCLC properties, as confirmed by the $I-V^2$ plots (Figure 1d, inset). The average value for V_{SCLC} was derived from the second-order differentiation of 1000 $I-V$ curves. For a 20 nm gap, the average V_{SCLC} was 5.5 ± 0.8 V.

This highly reproducible V_{SCLC} suggests that SCLC between the fixed nanogap electrodes occurred with reasonable reproducibility, depending on the nanogap width. The current in the PF regime exhibited only small variations, whereas large variations in the current were observed after switching to SCLC. However, the cause for this variation remains unknown.

The average V_{NDR} is plotted as a function of the gap width (measured using SEM) in Figure 2b. As the gap width increases, V_{NDR} increases, supporting the understanding that NDR is generated by the local heating effect through the conduction channel in an LRS.

The $I-V$ curves obtained from 1000 repeated measurements of the set process were also plotted, and the turn-on transition voltage ($V_{turn\text{-}on}$) was determined (Figure 2c). Although there were large differences in the initial currents, $V_{turn\text{-}on}$ was consistently 3.3 V and was independent of the gap width (Figure 2d). This suggests that the turn-on transition occurs because of the applied voltage between the disconnected conducting chains of the electrodes.

To analyze the reset process, $I-V$ plots measured for devices with different gap widths were characterized (Figure S4 in the Supporting Information). From these plots, V_{SCLC} values of 5.5 ± 0.8, 4.5 ± 0.6, and 4.0 ± 0.4 V were obtained for SEM-determined lengths of 20, 17, and 11 nm, respectively. These V_{SCLC} values were used to calculate the conduction path length (d) of the SCLC medium using the following formula:[51,52]

$$V_{SCLC} = \frac{qd^2 n_t}{2\varepsilon} \tag{1}$$

where n_t is the trap density, ε is the permittivity, and q is the elementary charge. The conduction path lengths for the M and S channel devices were calculated by normalizing the data with respect to the L channel device (assuming a nominal gap width of 20 nm). The trap densities of the three channels were assumed to be the same because the CPTA spin-coating conditions were the same. Then, the following relationship was used:

$$d_x^{\,2} = \frac{\varepsilon_x V_{SCLC_x}}{\varepsilon_{20} V_{SCLC_{20}}} d_{20}^{\,2} (x = \text{M or S}) \tag{2}$$

where d_{20}, ε_{20}, and V_{SCLC20} are the conduction path length, permittivity, and starting voltage of SCLC in the L (20 nm) channel, respectively. We did not use a specific value for the trap density because this was a relative length estimation. Although the permittivity (ε_x) in the CPTA films of all samples should be similar, experimental values were used to estimate d_x. The experimental ε_x values were extracted from the inverse gradients of the $I-V$ curve in the PF regime,[53] which varied slightly in each $I-V$ curve. The slight variations in the $I-V$ curves in the PF regime are attributed to local fluctuations in the degree of polymerization in and around the nanogap channel.

The extracted effective path lengths for the M and S channels were longer than the SEM-determined lengths (Table 1). This implies that the current did not flow through the shortest straight path in the image, where the electric field was intuitively concentrated. Instead, it meanders through tortuous conductive media composed of 1 nm spherical nanoparticles. This was attributed to the disordered fullerene arrangement in the amorphous film between the electrodes (in contrast to the ordered crystalline structure). Alternatively, it is possible that the point at which the current was injected into the media was the same as that assumed to calculate the shortest distance between the electrodess from the SEM images and that the other actual surface tip could not be resolved well by SEM.

Table 1. SEM-Determined Length, Average V_{SCLC}, and Effective Current Path Lengths Determined from V_{SCLC}[a]

	SEM-determined length (nm)	average V_{SCLC} (V)	path lengths extracted from V_{SCLC} (nm)
L (long)	20	5.5 ± 0.8	(20)
M (medium)	17	4.5 ± 0.6	18
S (short)	11	4.2 ± 0.4	14

[a]The effective current path is a relative length based on the measured width of the long channel. The average V_{SCLC} was derived from second-order differentiation of 1000 $I-V$ curves.

V_{NDR} and the required current (I_{NDR}) were extracted for each gap and plotted as histograms (Figure 3a,b). As the channel length

https://doi.org/10.1021/acsaelm.3c01656
ACS Appl. Electron. Mater. 2024, 6, 1740−1745

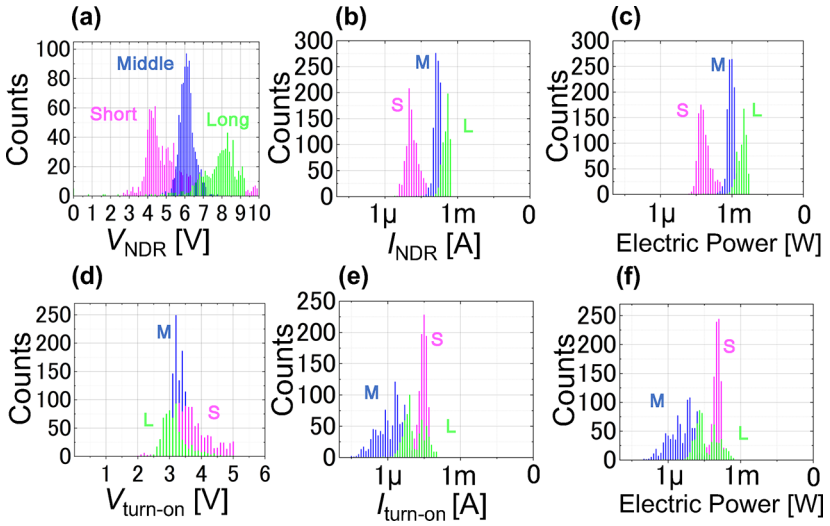

Figure 3. Turn-on properties and NDR distributions of devices with short (S), medium (M), and long (L) channels. (a) NDR voltage distribution, (b) current distribution, and (c) required power. (d) Turn-on voltage distribution, (e) current distribution, and (f) required power.

increases, the V_{NDR} and I_{NDR} also increase. The required NDR power ($V_{NDR} \times I_{NDR}$) is also plotted (Figure 3c). As expected from V_{NDR} and I_{NDR}, a longer channel requires greater power, and the electric power increases nonlinearly with the effective current path length (Figure 4).

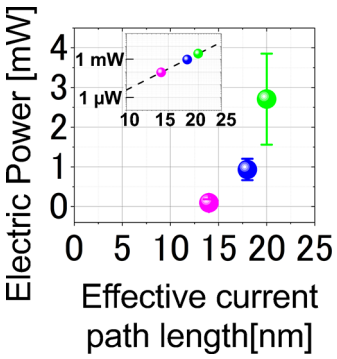

Figure 4. NDR generation power was calculated from V_{NDR} and I_{NDR} as a function of the effective current path length in the nanogap. Inset: log plot of NDR generation power used to estimate the required power for a minimum fullerene chain length.

This suggests that shorter current paths result in more efficient local heating and that the bonds in the C_{60} chain can be resolved by depolymerization. The gap-dependent power was linear when plotted logarithmically (Figure 4, inset), although the mechanism remains unknown. Extrapolation to the nanometer scale predicts that the required power is on the order of nanowatts. For example, a 2 nm gap should reduce the power to 0.24 pW. In contrast, the turn-on voltage was always observed at approximately 3.3 V regardless of the gap (Figure 3d), but there was no clear channel length dependence of the turn-on current (Figure 3e). These voltage and current results show that, although there is no clear channel length dependence, the required turn-on power is 1 order of magnitude lower than the NDR power (Figure 3f).

The effective conduction path length of the fullerene polymer chains introduced between the nanoscale electrodes was estimated by using SCLC. The effective path length was evaluated by averaging 1000 measurements of the voltage at which the SCLC appeared. This effective path length tends to be longer than the shortest distance between the electrodes obtained from the SEM images, presumably because of the tortuous path through the spherical fullerenes distributed in the amorphous film. Furthermore, the correlation between the path length and power required for NDR generated by heat near the channel was found to be logarithmic, indicating that nanowatt-scale (or lower) switch element operations can be expected in optimized nanometer-scale switching devices.

■ ASSOCIATED CONTENT

Supporting Information

The Supporting Information is available free of charge at https://pubs.acs.org/doi/10.1021/acsaelm.3c01656.

Additional experimental details and theoretical support of the experimental results. Figure S1. Comparison of SEM systems to confirm the nanogap size. Figure S2. *I*–*V* characteristics of nanogaps without or with a CPTA coating. Figure S3. Operating principles of fullerene nanochain switching. Figure S4. Gap width dependence of SCLC transition voltage (VSCLC) (PDF)

■ AUTHOR INFORMATION

Corresponding Authors

Hiroshi Suga − *Faculty of Engineering, Chiba Institute of Technology, Narashino, Chiba 275-0016, Japan; Research Center for Materials Nanoarchitectonics (MANA), National Institute for Materials Science (NIMS), Tsukuba, Ibaraki 305-0044, Japan;* orcid.org/0000-0003-4333-4898; Email: hiroshi-suga@it-chiba.ac.jp

Kazuhito Tsukagoshi − *Research Center for Materials Nanoarchitectonics (MANA), National Institute for Materials Science (NIMS), Tsukuba, Ibaraki 305-0044, Japan; Faculty of Engineering, Chiba Institute of Technology, Narashino, Chiba 275-0016, Japan;* orcid.org/0000-0001-9710-2692; Email: TSUKAGOSHI.Kazuhito@nims.go.jp

Authors

Masato Takei − *Faculty of Engineering, Chiba Institute of Technology, Narashino, Chiba 275-0016, Japan; Research Center for Materials Nanoarchitectonics (MANA), National Institute for Materials Science (NIMS), Tsukuba, Ibaraki 305-0044, Japan;* orcid.org/0000-0002-3522-0033

Takuma Hirama − *Faculty of Engineering, Chiba Institute of Technology, Narashino, Chiba 275-0016, Japan; Research Center for Materials Nanoarchitectonics (MANA), National*

https://doi.org/10.1021/acsaelm.3c01656
ACS Appl. Electron. Mater. 2024, 6, 1740−1745

Institute for Materials Science (NIMS), Tsukuba, Ibaraki 305-0044, Japan

Katsunori Wakabayashi − *Department of Nanotechnology for Sustainable Energy, School of Science and Technology, Kwansei Gakuin University, Sanda, Hyogo 669-1330, Japan;* orcid.org/0000-0002-9147-9939

Complete contact information is available at: https://pubs.acs.org/10.1021/acsaelm.3c01656

Author Contributions

M.T., T.H., and H.S. fabricated and measured the devices. K.W. and K.T. analyzed the conduction properties of a C_{60} polymer system. H.S. and K.T. conducted the experiments and prepared the manuscript. The manuscript was written with contributions from all the authors. All authors approved the final version of the manuscript. All authors contributed equally to this study.

Notes

The authors declare no competing financial interest.

■ ACKNOWLEDGMENTS

The authors would like to thank Y. Naitoh (AIST) for valuable discussions on binary switching operations. This study was supported by the JSPS KAKENHI (grant numbers 20K05291, 23K17869, and 19H05460), Japan.

■ ABBREVIATIONS

CPTA, C_{60} pyrrolidine tris-acid; PF, Poole−Frenkel; SCLC, space-charge-limited current; NDR, negative differential resistance; SEM, scanning electron microscopy; TEM, transmission electron microscopy; LRS, low-resistance state; HRS, high-resistance state

■ REFERENCES

(1) Ji, D.; Li, T.; Liu, J.; Amirjalayer, S.; Zhong, M.; Zhang, Z.-Y.; Huang, X.; Wei, Z.; Dong, H.; Hu, W.; Fuchs, H. Band-like Transport in Small-Molecule Thin Films toward High Mobility and Ultrahigh Detectivity Phototransistor Arrays. *Nat. Commun.* **2019**, *10*, 12.

(2) Naitoh, Y.; Shima, H.; Akinaga, H. Visualizing the Local Composition Changes during Resistive Switching in Planar TaO_x-ReRAMs. *ACS Appl. Electron. Mater.* **2023**, *5*, 4240−4247.

(3) Sahu, M. C.; Mallik, S. K.; Sahoo, S.; Gupta, S. K.; Ahuja, R.; Sahoo, S. Effect of Charge Injection on the Conducting Filament of Valence Change Anatase TiO_2 Resistive Random Access Memory Device. *J. Phys. Chem. Lett.* **2021**, *12* (7), 1876−1884.

(4) Sumi, M.; Satoh, N. Visualization of Current Distribution by Subsurface Magnetic Field Imaging System for the Cockcroft-Walton Circuit and Their Components. In *2021 IEEE 30th International Symposium on Industrial Electronics (ISIE)*; IEEE: Kyoto, Japan, 2021; pp 1−6.

(5) Wu, M.-C.; Chen, J.-Y.; Ting, Y.-H.; Huang, C.-Y.; Wu, W.-W. A Novel High-Performance and Energy-Efficient RRAM Device with Multi-Functional Conducting Nanofilaments. *Nano Energy* **2021**, *82*, No. 105717.

(6) Wei, Z.; Eriguchi, K. Analytic Modeling for Nanoscale Resistive Filament Variation in ReRAM With Stochastic Differential Equation. *IEEE Trans. Electron Devices* **2017**, *64*, 2201−2206.

(7) Shih, Y.-C.; Shen, Y.-C.; Cheng, Y.-K.; Chaudhary, M.; Yang, T.-Y.; Yu, Y.-J.; Chueh, Y.-L. Rational Design on Controllable Cation Injection with Improved Conductive-Bridge Random Access Memory by Glancing Angle Deposition Technology toward Neuromorphic Application. *ACS Appl. Mater. Interfaces* **2021**, *13*, 55470−55480.

(8) Deshmukh, S.; Rojo, M. M.; Yalon, E.; Vaziri, S.; Koroglu, C.; Islam, R.; Iglesias, R. A.; Saraswat, K.; Pop, E. Direct Measurement of Nanoscale Filamentary Hot Spots in Resistive Memory Devices. *Sci. Adv.* **2022**, *8*, 1514.

(9) Kondo, Y.; Takayanagi, K. Gold Nanobridge Stabilized by Surface Structure. *Phys. Rev. Lett.* **1997**, *79*, 3455−3458.

(10) Kasumov, A. Yu.; Tsukagoshi, K.; Kawamura, M.; Kobayashi, T.; Aoyagi, Y.; Senba, K.; Kodama, T.; Nishikawa, H.; Ikemoto, I.; Kikuchi, K.; Volkov, V. T.; Kasumov, Yu. A.; Deblock, R.; Guéron, S.; Bouchiat, H. Proximity Effect in a Superconductor-Metallofullerene-Superconductor Molecular Junction. *Phys. Rev. B* **2005**, *72*, No. 033414.

(11) Guo, Y.; Yang, C.; Zhang, L.; Guo, X. Tunable Interferometric Effects between Single-Molecule Suzuki−Miyaura Cross-Couplings. *J. Am. Chem. Soc.* **2023**, *145*, 6577−6584.

(12) Yang, Z.; Qi, C.; Liu, W.; Yin, D.; Yu, L.; Li, L.; Guo, X. Revealing Conformational Transition Dynamics of Photosynthetic Proteins in Single-Molecule Electrical Circuits. *J. Phys. Chem. Lett.* **2021**, *12*, 3853−3859.

(13) Umeta, Y.; Suga, H.; Takeuchi, M.; Zheng, S.; Wakahara, T.; Naitoh, Y.; Tsukagoshi, K. C_{60} -Nanowire Two-State Resistance Switching Based on Fullerene Polymerization/Depolymerization. *ACS Appl. Nano Mater.* **2021**, *4*, 820−825.

(14) Takeuchi, M.; Umeta, Y.; Suga, H.; Wakahara, T.; Wang, Y.-C.; Naitoh, Y.; Wakabayashi, K.; Tsukagoshi, K. Fullerene Nanostructure-Coated Channels Activated by Electron Beam Lithography for Resistance Switching. *ACS Appl. Nano Mater.* **2022**, *5*, 6430−6437.

(15) Azimi, H.; Senes, A.; Scharber, M. C.; Hingerl, K.; Brabec, C. J. Charge Transport and Recombination in Low-Bandgap Bulk Heterojunction Solar Cell Using Bis-adduct Fullerene. *Adv. Energy Mater.* **2011**, *1*, 1162−1168.

(16) Lin, G.; Lin, Y.; Huang, H.; Cui, R.; Guo, X.; Liu, B.; Dong, J.; Guo, X.; Sun, B. Novel Exciton Dissociation Behavior in Tin-Lead Organohalide Perovskites. *Nano Energy* **2016**, *27*, 638−646.

(17) Yen, T. J.; Chin, A.; Gritsenko, V. High Performance All Nonmetal SiN_x Resistive Random Access Memory with Strong Process Dependence. *Sci. Rep.* **2020**, *10*, 2807.

(18) Huang, Y.-J.; Lee, S.-C. Graphene/h-BN Heterostructures for Vertical Architecture of RRAM Design. *Sci. Rep.* **2017**, *7*, 9679.

(19) Bharathi, M.; Balraj, B.; Sivakumar, C.; Wang, Z.; Shuai, J.; Ho, M.-S.; Guo, D. Effect of Ag Doping on Bipolar Switching Operation in Molybdenum Trioxide (MoO_3) Nanostructures for Non-Volatile Memory. *J. Alloys Compd.* **2021**, *862*, No. 158035.

(20) Sivakumar, C.; Tsai, G.-H.; Chung, P.-F.; Balraj, B.; Lin, Y.-F.; Ho, M.-S. High-Quality Single-Crystalline β-Ga_2O_3 Nanowires: Synthesis to Nonvolatile Memory Applications. *Nanomaterials* **2021**, *11*, 2013.

(21) Abbaszadeh, D.; Kunz, A.; Kotadiya, N. B.; Mondal, A.; Andrienko, D.; Michels, J. J.; Wetzelaer, G.-J. A. H.; Blom, P. W. M. Electron Trapping in Conjugated Polymers. *Chem. Mater.* **2019**, *31*, 6380−6386.

(22) Mu, B.; Hsu, H.-H.; Kuo, C.-C.; Han, S.-T.; Zhou, Y. Organic Small Molecule-Based RRAM for Data Storage and Neuromorphic Computing. *J. Mater. Chem. C* **2020**, *8*, 12714−12738.

(23) Yuan, Y.; Wang, Y.; Tang, X.; Zhang, N.; Zhang, W. Enhanced Resistive Switching Performance through Air-Stable Cu_2AgSbI_6 Thin Films for Flexible and Multilevel Storage Application. *ACS Appl. Mater. Interfaces* **2022**, *14*, 53990−53998.

(24) Takei, M.; Takeuchi, M.; Suga, H.; Wakahara, T.; Wakabayashi, K.; Okada, S.; Tsukagoshi, K. Electromechanical Switching of a C_{60} Chain in a Nanogap. *ACS Appl. Electron. Mater.* **2023**, *5*, 3184−3189.

(25) Suga, H.; Suzuki, H.; Otsu, K.; Abe, T.; Umeta, Y.; Tsukagoshi, K.; Sumiya, T.; Shima, H.; Akinaga, H.; Naitoh, Y. Feedback Electromigration Assisted by Alternative Voltage Operation for the Fabrication of Facet-Edge Nanogap Electrodes. *ACS Appl. Nano Mater.* **2020**, *3*, 4077−4083.

(26) Liu, J. High-Resolution and Low-Voltage FE-SEM Imaging and Microanalysis in Materials Characterization. *Mater. Charact.* **2000**, *44*, 353−363.

(27) Huang, S.-K.; Wang, Y.-C.; Ke, W.-C.; Kao, Y.-T.; She, N.-Z.; Li, J.-X.; Luo, C.-W.; Yabushita, A.; Wang, D.-Y.; Chang, Y. J.;

Tsukagoshi, K.; Chen, C.-W. Unravelling the Origin of the Photocarrier Dynamics of Fullerene-Derivative Passivation of SnO_2 Electron Transporters in Perovskite Solar Cells. *J. Mater. Chem. A* **2020**, *8*, 23607−23616.
(28) Rietmeijer, F. J. M. Are crystalline C-(H-O-N) carbons the elusive meteoritic carbynes? *Meteoritics* **1993**, *28*, 242−245.
(29) Xie, X.; Li, P.; Xu, Y.; Zhou, L.; Yan, Y.; Xie, L.; Jia, C.; Guo, X. Single-Molecule Junction: A Reliable Platform for Monitoring Molecular Physical and Chemical Processes. *ACS Nano* **2022**, *16*, 3476−3505.
(30) Chandler, H. J.; Stefanou, M.; Campbell, E. E. B.; Schaub, R. Li@C_{60} as a Multi-State Molecular Switch. *Nat. Commun.* **2019**, *10*, 2283.
(31) Du, S.; Hashikawa, Y.; Ito, H.; Hashimoto, K.; Murata, Y.; Hirayama, Y.; Hirakawa, K. Inelastic Electron Transport and Ortho−Para Fluctuation of Water Molecule in H_2O@C_{60} Single Molecule Transistors. *Nano Lett.* **2021**, *21*, 10346−10353.
(32) Yasuraoka, K.; Kaneko, S.; Kobayashi, S.; Tsukagoshi, K.; Nishino, T. Surface-Enhanced Raman Scattering Stimulated by Strong Metal- Molecule Interactions in a C_{60} Single-Molecule Junction. *ACS Appl. Mater. Interface.* **2021**, *13*, 51602−51607.
(33) Fujii, S.; Cho, H.; Hashikawa, Y.; Nishino, T.; Murata, Y.; Kiguchi, M. Tuneable Single-Molecule Electronic Conductance of C_{60} by Encapsulation. *Phys. Chem. Chem. Phys.* **2019**, *21*, 12606−12610.
(34) Ryu, T.; Lansac, Y.; Jang, Y. H. Shuttlecock-Shaped Molecular Rectifier: Asymmetric Electron Transport Coupled with Controlled Molecular Motion. *Nano Lett.* **2017**, *17*, 4061−4066.
(35) Chikamatsu, M.; Nagamatsu, S.; Yoshida, Y.; Saito, K.; Yase, K.; Kikuchi, K. Solution-Processed n-Type Organic Thin-Film Transistors with High Field-Effect Mobility. *Appl. Phys. Lett.* **2005**, *87*, 203504.
(36) Kubozono, Y.; Haas, S.; Kalb, W. L.; Joris, P.; Meng, F.; Fujiwara, A.; Batlogg, B. High-Performance C_{60} Thin-Film Field-Effect Transistors with Parylene Gate Insulator. *Appl. Phys. Lett.* **2008**, *93*, No. 033316.
(37) Xu, T.; Yin, H.; Yu, P.; He, Z.; Chen, N.; Shen, W.; Zhu, M.; Akasaka, T.; Lu, X. Ultraviolet Photodetectors Based on Dimetallofullerene Lu_2@C_s(6)-C_{82} Nanorods. *ACS Appl. Nano Mater.* **2022**, *5*, 1683−1689.
(38) Tan, J.; Sorensen, J.; Dong, H.; Hu, W. Fullerene-Derivative as Interlayer for High Performance Organic Thin-Film Transistors. *J. Mater. Chem. C* **2018**, *6*, 6052−6057.
(39) Zhao, X.; Liu, T.; Liu, H.; Wang, S.; Li, X.; Zhang, Y.; Hou, X.; Liu, Z.; Shi, W.; Dennis, T. J. S. Organic Single-Crystalline p−n Heterojunctions for High-Performance Ambipolar Field-Effect Transistors and Broadband Photodetectors. *ACS Appl. Mater. Interfaces* **2018**, *10*, 42715−42722.
(40) Zhao, X.; Liu, T.; Cui, Y.; Hou, X.; Liu, Z.; Dai, X.; Kong, J.; Shi, W.; Dennis, T. J. S. Antisolvent-Assisted Controllable Growth of Fullerene Single Crystal Microwires for Organic Field Effect Transistors and Photodetectors. *Nanoscale* **2018**, *10*, 8170−8179.
(41) Frolova, L. A.; Furmansky, Y.; Shestakov, A. F.; Emelianov, N. A.; Liddell, P. A.; Gust, D.; Visoly-Fisher, I.; Troshin, P. A. Advanced Nonvolatile Organic Optical Memory Using Self-Assembled Monolayers of Porphyrin−Fullerene Dyads. *ACS Appl. Mater. Interfaces* **2022**, *14*, 15461−15467.
(42) Umeta, Y.; Suga, H.; Takeuchi, M.; Zheng, S.; Wakahara, T.; Wang, Y.-C.; Naitoh, Y.; Lu, X.; Kumatani, A.; Tsukagoshi, K. Stable Resistance Switching in Lu_3N@C_{80} Nanowires Promoted by the Endohedral Effect: Implications for Single-Fullerene Motion Resistance Switching. *ACS Appl. Nano Mater.* **2021**, *4*, 7935−7942.
(43) Qi, D.; Zhang, L.; Wan, L.; Zhao, L.; Jiang, J. Design of a Universal Reversible Bidirectional Current Switch Based on the Fullerene−Phthalocyanine Supramolecular System. *J. Phys. Chem. A* **2012**, *116*, 6785−6791.
(44) Liedtke, M.; Sperlich, A.; Kraus, H.; Baumann, A.; Deibel, C.; Wirix, M. J. M.; Loos, J.; Cardona, C. M.; Dyakonov, V. Triplet Exciton Generation in Bulk-Heterojunction Solar Cells Based on Endohedral Fullerenes. *J. Am. Chem. Soc.* **2011**, *133*, 9088−9094.
(45) Huang, P.-C.; Huang, S.-K.; Lai, T.-C.; Shih, M.-C.; Hsu, H.-C.; Chen, C.-H.; Lin, C.-C.; Chiang, C.-H.; Lin, C.-Y.; Tsukagoshi, K.; Chen, C.-W.; Chiu, Y.-P.; Tsay, S.-F.; Wang, Y.-C. Visualizing Band Alignment across 2D/3D Perovskite Heterointerfaces of Solar Cells with Light-Modulated Scanning Tunneling Microscopy. *Nano Energy* **2021**, *89*, No. 106362.
(46) Xue, D.; Wakahara, T.; Marumoto, K.; Tsukagoshi, K. High Charge Transfer from C_{60} Pyrrolidine Tris-Acid to SnO_2 Electron Transport Layer Directly Observed by ESR Spectroscopy. *ACS Appl. Energy Mater.* **2023**, *6*, 2434−2439.
(47) Frenkel, J. On Pre-Breakdown Phenomena in Insulators and Electronic Semi-Conductors. *Phys. Rev.* **1938**, *54*, 647−648.
(48) Nouchi, R.; Masunari, K.; Ohta, T.; Kubozono, Y.; Iwasa, Y. Ring of C_{60} Polymers Formed by Electron or Hole Injection from a Scanning Tunneling Microscope Tip. *Phys. Rev. Lett.* **2006**, *97*, No. 196101.
(49) Okada, S.; Kowashi, S.; Schweighauser, L.; Yamanouchi, K.; Harano, K.; Nakamura, E. Direct Microscopic Analysis of Individual C_{60} Dimerization Events: Kinetics and Mechanisms. *J. Am. Chem. Soc.* **2017**, *139*, 18281−18287.
(50) Nakaya, M.; Aono, M.; Nakayama, T. Ultrahigh-Density Data Storage into Thin Films of Fullerene Molecules. *Jpn. J. Appl. Phys.* **2016**, *55*, No. 1102B4.
(51) Chiu, F.-C. A Review on Conduction Mechanisms in Dielectric Films. *Adv. Mater. Sci. Eng.* **2014**, *2014*, 1−18.
(52) Bhutta, M. S.; Akram, S.; Meng, P.; Castellon, J.; Agnel, S.; Li, H.; Guo, Y.; Rasool, G.; Hussain, S.; Nazir, M. T. Steady-State Conduction Current Performance for Multilayer Polyimide/SiO_2 Films. *Polymers* **2021**, *13*, 640.
(53) Al-Harthi, A. M.; Mahmoud, W. E. Influence of the Fullerene Acceptor Derivative on the Structure, Molecular Interaction and Optoelectronic Properties of Poly(3-Hexylthiophene) Blend Films: Elucidating Key Factors. *Opt. Mater.* **2022**, *124*, No. 112009.

https://doi.org/10.1021/acsaelm.3c01656
ACS Appl. Electron. Mater. 2024, 6, 1740−1745